



UNIVERSITY OF LEEDS

This is a repository copy of *Real-time monitoring of fat crystallization using pulsed acoustic spectroscopy and supervised machine learning*.

White Rose Research Online URL for this paper:

<https://eprints.whiterose.ac.uk/216949/>

Version: Accepted Version

Article:

Metilli, L., Morris, L., Lazidis, A. et al. (4 more authors) (2022) Real-time monitoring of fat crystallization using pulsed acoustic spectroscopy and supervised machine learning. *Journal of Food Engineering*, 335. 111192. ISSN 0260-8774

<https://doi.org/10.1016/j.jfoodeng.2022.111192>

© 2022 Elsevier. This is an author produced version of an article accepted for publication in *Journal of Food Engineering*. Uploaded in accordance with the publisher's self-archiving policy. This manuscript version is made available under the CC-BY-NC-ND 4.0 license <http://creativecommons.org/licenses/by-nc-nd/4.0/>.

Reuse

Items deposited in White Rose Research Online are protected by copyright, with all rights reserved unless indicated otherwise. They may be downloaded and/or printed for private study, or other acts as permitted by national copyright laws. The publisher or other rights holders may allow further reproduction and re-use of the full text version. This is indicated by the licence information on the White Rose Research Online record for the item.

Takedown

If you consider content in White Rose Research Online to be in breach of UK law, please notify us by emailing eprints@whiterose.ac.uk including the URL of the record and the reason for the withdrawal request.



eprints@whiterose.ac.uk
<https://eprints.whiterose.ac.uk/>

1 Real-time monitoring of fat crystallization using
2 pulsed acoustic spectroscopy and supervised machine
3 learning

4 *Lorenzo Metilli¹, Liam Morris¹, Aris Lazidis², Stephanie Marty-Terrade³, Melvin Holmes¹,*
5 *Megan Povey¹ and Elena Simone^{1,4}*

6 ¹ School of Food Science and Nutrition, Food Colloids and Bioprocessing group, University of
7 Leeds, Woodhouse Lane, Leeds LS2 9JT, UK

8 ² Nestlé Product Technology Centre Confectionery, Haxby Road, York YO31 8TA, UK

9 ³ Nestlé Research, Vers-chez-les-Blanc, 1000 Lausanne 26, Switzerland

10 ⁴ Department of Applied Science and Technology (DISAT), Politecnico di Torino, Torino (Italy)

11

12 KEYWORDS

13 Crystallization, Fats, Oils, Ultrasound, Machine Learning

14

15 ABSTRACT

16

17 Enhancing the control and yield of lipid crystallization is fundamental in several industrial areas,
18 including pharmaceutical, cosmetic and food manufacturing. However, the multi-component
19 nature of fats and oils poses a challenge in the understanding and control of the final product
20 properties. While the crystallization of lipid has been extensively studied with offline techniques,
21 online monitoring of the process would be highly advantageous, especially in large-scale sheared
22 vessels. In this work, a novel method to calculate the solid fat content (SFC%) of crystallizing
23 lipids under shear, based on an acoustic probe and supervised-machine learning, is presented. The
24 temperature, composition and ultrasonic velocity of the samples, and the SFC(%) measured with
25 nuclear magnetic resonance were used to develop a predictive model to calculate the SFC(%)
26 during crystallization. Gaussian models showed the highest accuracy compared to linear and
27 regression tree models (RMSE = 0.03 vs 0.7 and 0.25, respectively).

28 **1. Introduction**

29 The crystallization of lipids is a fundamental unit operation for several manufacturing industries,
30 including pharmaceuticals (Jose & Netto, 2019), cosmetic (Duprat-De-Paule et al., 2018; Patel et
31 al., 2021) and food (Rios et al., 2014). Recently, the use of crystalline fat to produce structured
32 oils (oleogels) has gained significant attention from academia and industry alike, due to the
33 potential to produce solid-like materials with low amounts of saturated fat and specific
34 macroscopic properties (Patel & Dewettinck, 2016). Furthermore, oleogels may be used as
35 precursors for the production of oil-continuous foams (Binks & Vishal, 2021) and emulsified oil
36 foams (Brun et al., 2015; Goibier et al., 2019) that can find application as nutrients or drug delivery
37 vehicles, or as structuring materials for food products. In all of the above examples, the properties
38 of the fat crystals, such as crystal size, shape and polymorphism, significantly affect the stability
39 and functionality (*e.g.*, drug delivery, oil binding capacity, air incorporation) of the final oleogel

40 material (Co & Marangoni, 2012; Heymans et al., 2017). The total amount of crystals, *i.e.* the solid
41 fat content (*SFC%*), is a general parameter strongly related to some macroscopic properties of fat-
42 based materials, such as the melting point, hardness and texture (Himawan et al., 2006). Hence,
43 monitoring *SFC%* during crystallization processes is important to determine when equilibrium
44 conditions are reached, and therefore maximize the yield of crystallization in industrial contexts.

45 The *SFC%* is routinely measured by means of nuclear magnetic resonance (NMR) (Cerdeira et al.,
46 2004), differential scanning calorimetry (DSC) (Foubert et al., 2008) or small-angle X-Ray
47 scattering (SAXS) (Ladd Parada et al., 2019). These techniques, however, are all off-line, requiring
48 the collection of a sample (not always a trivial operation, especially if the sample melting point is
49 close to ambient temperature) and some degree of sample preparation, which can significantly
50 affect the measurement. In the context of industrial large-scale crystallization, the issues related to
51 off-line analysis and sampling are tackled by applying process analytical technology (PAT) tools,
52 which enable real-time monitoring of the product properties, enhanced process understanding, and
53 the application of the so called “Quality by Design” (QbD) strategy (Rathore et al., 2010).
54 Common PAT tools used to monitor crystallization usually include *in situ* probes that exploit the
55 scattering or absorption of electromagnetic radiation (visible light, ultra-violet (UV) or infra-red)
56 by the sample to monitor phase transitions, polymorphic transformations or crystal morphology
57 (Hansen et al., 2017; Simone et al., 2015; Simone et al., 2019). In the case of industrial lipid
58 crystallization, online determination of the *SFC%* is highly sought, albeit presenting some
59 challenges. Fat crystals form a viscous three-dimensional network of aggregates with a fractal
60 pattern (Tang & Marangoni, 2008), whose quantification is non-trivial. Moreover, (partially)
61 crystalline fat is often opaque to electromagnetic radiation, limiting the analysis to the surface of
62 the sample. While oleogels (and hydrogels) are widely used in consumer products, at present there

63 are sparse examples of PAT tools applied to the manufacturing process of materials with similar
64 properties (Bostijn et al., 2018; Pu et al., 2015).

65 The use of low-power ultrasound for studying the crystallization of lipids has been proposed as a
66 non-invasive, non-destructive method since the 1980s (Hussin & Povey, 1984; McClements &
67 Povey, 1988; McClements & Povey, 1987). Low-power ultrasound, *i.e.*, sound waves exceeding
68 20 kHz frequency, can penetrate opaque media, without causing physical and chemical changes in
69 the sample. Moreover, it is relatively inexpensive compared to other spectroscopy techniques, and
70 it is easily adaptable to different measuring configurations (Povey, 2017). The technique involves
71 the propagation of a short (few microseconds) ultrasonic pulse from a transducer into the sample;
72 this pulse is received by either another transducer on the other side of the measuring apparatus
73 (pitch-and-catch mode) or it is reflected and received by the same emitting transducer (pulse-echo
74 mode). The velocity of sound (c_{sample}) is then calculated from the travelled path length as a function
75 of time and temperature. The acoustic attenuation (α), *i.e.*, the ratio of the amplitude of the sent
76 and received pulse, may also be calculated. As both the velocity of sound and acoustic attenuation
77 depend on the physicochemical properties of the sample, such as density and adiabatic
78 compressibility, and the presence of heterogeneities, acoustic measurements can be used to
79 monitor phase transitions such as crystallization and polymorphic transformations (Fairley &
80 McClements, 1992; Kloek et al., 2000; Miles et al., 1985). Several authors demonstrated the use
81 of custom-made acoustic cells to study fat crystallization using acoustic signals, with particular
82 emphasis on determining the *SFC*(%) (Birkhofer et al., 2008; Martini et al., 2005a, Martini et al.,
83 2005b; Singh et al., 2002, Singh et al., 2004). Nevertheless, most of the previous works on fat
84 crystallization were carried out in quiescent conditions, and/or with small sample volumes, thus

85 excluding the effect of shear and secondary nucleation on crystallization which are predominant
86 on industrial scale (Agrawal & Paterson, 2015).

87 Despite its several advantages and ease of implementation, there are only sporadic examples in the
88 literature on the use of acoustic probes as a PAT tool for studying lipid crystallization. The
89 immersion probe described in Titiz-Sargut & Ulrich (2003), which featured two 2 MHz
90 transducers in pitch-and-catch mode, was applied to the determination of the metastable zone
91 width (MSZW) of coconut oil, and validated by optical back-reflectance measurements (ORM)
92 (Chaleepa et al., 2010). The authors focused their study on the effect of different levels of shear,
93 cooling rates and the presence of additives on the MSZW; however, no quantitative information
94 on the *SFC%* of this lipid system was reported. Due to the complexity involved in the
95 crystallization of lipids, such as the occurrence of melt-mediated polymorphic transformations,
96 and the development of crystalline networks whose size range from nanometres to several
97 hundreds of microns, the determination of the *SFC%* directly from acoustic parameters is non-
98 trivial. Moreover, the large acoustic attenuation exhibited by crystalline fat results often in loss of
99 the acoustic signal (Rigolle et al., 2018). One of the growing trends in the use of PAT tools is the
100 implementation of machine learning (ML) algorithms to facilitate analysis of real-time data
101 provided by sensors, and to enable prediction of material properties of interest based on training
102 the algorithm with known outcomes (supervised machine learning) (Wasalathanthri et al., 2020).
103 Examples of ML applications in the context of crystallization include the automatic detection of
104 crystal aggregation from microscopic images (Ochsenbein et al., 2015), the real-time estimation
105 of the crystal size distribution of 2D needle-shaped crystals from measurements of chord length
106 and aspect ratio distributions (Szilágyi & Nagy, 2018) and the estimation of the 3D size
107 distribution of plate-like particles using projections from multiple cameras (Jaeggi et al., 2021).

108 The approach can be extended to the actual control of crystallization processing, for example
109 through the use of convolutional neural network (CNN) feedback control to dissolve undesired
110 precipitated impurities during the crystallization of active pharmaceutical ingredients (APIs)
111 (Salami et al., 2021). Recently, ML has been applied to ultrasonic reflectance measurements to
112 monitor the mixing process in a large-scale vessel (Bowler et al., 2020; Bowler & Watson, 2021).

113 In this work, a novel technique for estimating the *SFC%*, based on a custom-built acoustic probe
114 (Morris et al., 2021) and supervised machine learning is presented. This immersion acoustic probe
115 was used as a PAT sensor to monitor the crystallization of a cocoa butter/sunflower oil oleogel
116 system, in a 1L scale vessel and under shear. Cocoa butter and sunflower oil are both ingredients
117 widely used in food, cosmetic and pharmaceutical applications (Metilli et al., 2021). The ultrasonic
118 data was validated with light turbidimetry, and the *SFC%* of the crystallized oleogel was measured
119 with offline pulsed NMR (*p*NMR) at equilibrium conditions and specific temperatures. Finally,
120 supervised machine learning was applied to develop a predictive model based on the acoustic
121 parameters and the results of *p*NMR, enabling the calculation of *SFC%* based on the velocity of
122 sound, sample composition and temperature.

123 **2. Materials and Methods**

124 **2.1 Cocoa butter–based oleogels**

125 Refined, bleached and deodorized cocoa butter (CB) and high-oleic sunflower oil (HOSO) were
126 kindly provided by Nestlé PTC Confectionery (York, UK) and used without any further
127 purification. CB was melted at 65 °C for one hour, and then mixed with HOSO at 9%, 11%, 13%
128 and 15% concentration by weight. HOSO contains usually the following fatty acids (by weight):
129 86% oleic acid, 5% stearic acid, 3% linoleic acid, 3% palmitic acid, 1.5% behenic acid, and 0.7%

130 arachidic acid (Fernández-Moya et al., 2000). CB normally contains by a weight about 26%
131 palmitic acid, 36% stearic acid, 34% oleic acid, 2.7% linoleic, and 0.9% arachidic acid (Lipp et
132 al., 2001).

133 **2.2 Fat crystallization rig**

134 The CB-HOSO mixture (900 g) was transferred to a jacketed crystallization vessel (capacity *ca.* 1
135 L, diameter 15 cm) (Radley, UK) connected to a Huber Ministat 230 thermostat (Huber, Germany),
136 filled with silicone oil as a heating/cooling medium. The sample was stirred continuously at 200
137 rpm with a DLH overhead stirrer (VELP Scientifica, Italy), equipped with an anchor-shaped mixer
138 (8 cm diameter). A Pt-100 temperature probe (Omega Engineering, UK), placed in the vessel, was
139 used to monitor the sample temperature during the experiment. The crystallization process was
140 followed using a Control 4000 turbidity meter (Optek, Germany) fitted with an ASD12-N
141 absorption probe, which measured light transmittance and absorbance. Finally, the velocity of
142 sound and the acoustic attenuation of the crystallizing mixture were measured using a custom
143 acoustic probe, recently described in literature (Morris et al., 2021), with some design
144 modifications. Briefly, the probe comprised a 2.25 MHz broadband transducer coupled with a
145 Rexolite buffer rod (Sonatest model RDT5025, Sonatest, UK), and a stainless-steel acoustic
146 reflector plate. This probe was manufactured in an ‘L’ shape configuration. The probe was
147 connected to a UT320 pulser/receiver (UTEX scientific instruments inc., Canada) and a HDO3034
148 digital oscilloscope (Teledyne LeCroy, USA). A schematic of the equipment is shown in Figure
149 1.

150 The thermal profile of the experiment was set to the following: Equilibration of the fat blend
151 mixture at 45 °C for 10 minutes, cooling to 0 °C at a nominal rate of –0.5 °C/min and holding at

152 0°C for 3 hours. The sample was then heated back to 45 °C at 1 °C/min. The process temperature
153 and the acoustic waveforms were collected using an in-house script developed with
154 MATLAB2021a (MathWorks, USA). Measurements were collected every 10 seconds. Each
155 experiment was repeated three times.

156 **2.3 Determination of the acoustic parameters**

157 **2.3.1 Velocity of Sound**

158 Figure contains a diagram describing the design of the acoustic probe, and an example of
159 waveform acquired from the oscilloscope with MATLAB.

160 The ultrasonic pulse generated from the transducer travels through the buffer rod, and it is partially
161 reflected at the buffer rod/sample interface, due to the acoustic impedance mismatch (*i.e.*, the
162 difference in the product of density and velocity of sound of the two materials). The pulse is then
163 received back by the transducer after a time Δt_1 , shown in Figure as the blue trace. Part of the
164 initial pulse, however, is transmitted through the sample, and it is reflected by the stainless-steel
165 reflector to the transducer after a time Δt_2 (Figure , red trace). In order to calculate the velocity of
166 sound in the sample, the time of flight in the sample is required. To calculate it, the initial value of
167 Δt_1 and Δt_2 were first determined with MATLAB2021a from the original waveform, using the
168 leading-edge method (*i.e.*, detecting the arrival time of the pulse envelope when it crosses a set
169 voltage threshold). Afterwards, the shifts of the pulses' position ($\Delta\Delta t_1$ and $\Delta\Delta t_2$) during the
170 experiment were calculated with the cross-correlation function (*xcorr*) implemented in MATLAB.
171 This function provides an estimate of the correlation between each analysed waveform and a
172 reference waveform, returning the intensity of the correlation value as a function of time units. The
173 position of the maximum peak of this calculated vector corresponds to the time delay between two
174 pulses. This method proved to be more robust in the analysis of the set of waveforms compared to

175 applying the leading-edge technique on all collected waveforms. This is because the pulse envelop
 176 was subject to distortion due to frequency dependent signal attenuation through the experiment.
 177 The variation in the sample time of flight ($\Delta\Delta t_3$) was then calculated with Equation 1:

$$\Delta\Delta t_3 = \Delta\Delta t_2 - \Delta\Delta t_1 \quad (\text{Eq. 1})$$

178 In order to obtain an accurate value of the velocity of sound, however, it was necessary to
 179 determine the path length dependence on the temperature with a calibration experiment. The
 180 velocity of sound in distilled water (c_{water}) with respect to temperature (T) may be calculated using
 181 a fifth-order polynomial, as first described by Chávez et al. (1985) (Equation 2):

$$c_{\text{water}} = 3.16 \cdot 10^{-9}T^5 - 1.48 \cdot 10^{-6}T^4 + 3.35 \cdot 10^{-4}T^3 - 5.81 \cdot 10^{-2}T^2 + 5.04 \cdot T + 1.40 \cdot 10^3 \quad (\text{Eq. 2})$$

182 The shift in the time of flight in distilled water ($\Delta\Delta t_{3,\text{water}}$) was then measured between 50 °C and
 183 5°C, using a -0.01 °C/min cooling rate to allow the probe to reach thermal equilibrium with the
 184 surrounding medium. The corresponding experimental path length ($L_{\text{calibrated}}$) was calculated with
 185 Equation 3

$$L_{\text{calibrated}} = \Delta\Delta t_{3,\text{water}} \times c_{\text{water}} \quad (\text{Eq. 3})$$

186 The dependence of the path length on the temperature was then obtained by fitting a fifth-order
 187 polynomial to $L_{\text{calibrated}}$ against the temperature (Figure).

188 The coefficients estimated for the path length calculation were then used to accurately calculate
 189 the velocity of sound during the crystallization experiments with Equation 4

$$c_{\text{sample}} = \frac{L_{\text{calibrated}}}{\Delta\Delta t_3} \quad (\text{Eq. 4})$$

190 **2.3.2 Acoustic Attenuation**

191 The acoustic attenuation quantifies the acoustic power absorbed and scattered by the sample, and
 192 is affected by several factors, including the onset of phase transitions and scattering phenomena

193 generated by the presence of dispersed objects in the sample (McClements & Povey, 1992). In this
194 work, the acoustic attenuation was used to detect the onset of crystal growth and dissolution during
195 the crystallization experiments. The acoustic attenuation was calculated according to Equation 5

$$\alpha = -20 \log \frac{A}{A_0} \quad (\text{Eq. 5})$$

196 where A and A_0 are the peak-to-peak amplitudes of the sample signal during the experiment, and
197 at the start of the experiment, respectively.

198

199 **2.3.3 Solid Fat Content**

200 The solid fat content ($SFC\%$), defined as the mass fraction of solid to liquid material in a fat blend,
201 was calculated by applying a prediction model, developed with the Regression Learner App in
202 MATLAB2021a, (MathWorks, USA). Regression Learner is a supervised machine-learning
203 utility, where a regression algorithm is applied to an observation matrix and compared with a
204 response matrix. The observation matrix comprised the temperature (T), velocity of sound in the
205 sample (c_{sample}) and the amount of added cocoa butter ($CB\%$) for each crystallization experiment;
206 the response matrix contained the $SFC\%$ values, measured with pNMR, between 5 and 45 °C for
207 the respective samples. The velocity of sound and temperature of pure sunflower oil were also
208 added to the observation matrix, with a corresponding solid fat content of 0%. The sunflower oil
209 data was included in the model to provide information on the behaviour of a sample without any
210 crystallizing material in the explored experimental conditions. Three models available in the
211 Regression Learner App were tested for training of the dataset, and their predictive ability were
212 compared: “Linear”, “Fine Tree” and “Gaussian Process Regression–Rational Quadratic”. The
213 Linear model uses a linear regression to fit the data from the observation matrix. The “Fine Tree”
214 model, instead, is a type of nonlinear model based on regression trees, which applies a recursive

215 partition of the observation matrix to improve the prediction of the response value. Lastly, the
216 Gaussian Process Regression model, which is also nonlinear, works by predicting the probability
217 distribution of responses for each parameter in the observation matrix. Model cross-validation was
218 performed using the in-built function in the Regression Learner App (5-fold validation setting).
219 Briefly, the software divides the dataset into a number of sub-sets of the same size, trains the
220 predictive model on all sub-sets except one, which is used as test data. This process is repeated
221 until all sub-sets have been used as test data once (Bosnić & Kononenko, 2009). The accuracy of
222 all iterations is calculated as R^2 , RMSE and other statistical parameters. In the discussion, the Root
223 Mean Square Error values (RMSE) were compared to select the most accurate predictive model.

224

225 **2.4 Pulsed Nuclear Magnetic Resonance (pNMR)**

226 The solid fat content (*SFC*%) of the CB-HOSO mixtures was determined with *p*NMR using a
227 Bruker Minispec NMR (Bruker, Switzerland). The samples were collected at the end of the
228 crystallization experiment, transferred to a 10 mm inner diameter NMR tube and stored in a fridge
229 at 4 °C. The *SFC*% was measured between 5 and 45 °C, in steps of 5 °C. During the experiment,
230 the NMR tube was left to equilibrate for 90 minutes for each temperature step. The measurements
231 were carried out in triplicates. The resulting *SFC*(%) vs. temperature data was fitted using a
232 Gompertz-type model (Farmani, 2015) to obtain the *SFC*(%) as a function of the temperature and
233 CB%.

234 **3. Results and Discussion**

235 **3.1 Fat crystallization monitored by PAT tools**

236 The crystallization of one 9% CB w/w in HOSO sample, monitored with turbidity and the acoustic
237 probe, is shown in Figure 4.

238 While some variability among the three experiments conducted for each CB concentration was
239 observed, (particularly in the crystallization temperature and the absolute values of acoustic
240 attenuation) the trends observed for all CB/HOSO samples were similar. In particular, for the
241 experiment shown in Figure 4a, four regions could be identified. Between 0 and 115 minutes
242 (region I of Figure 4a) the temperature of the sample followed the cooling profile, from 45 °C to
243 5°C, accompanied by an increase in the velocity of sound, from 1390 to 1510 m/s, due to the
244 negative velocity coefficient with respect to temperature (McClements & Povey, 1992). After 115
245 minutes, when the sample temperature reached 5 °C, the onset of nucleation was detected by a
246 sharp decrease in the light transmittance, due to the sample becoming turbid (region II).
247 Simultaneously, the light absorbance increased, exhibiting two distinct steps: a first, modest
248 increase occurring between 115 and 129 minutes, and a larger increase after 129 minutes.
249 Interestingly, the acoustic attenuation and the velocity of sound were responsive to the second step
250 only, with a delay in detecting the onset of crystallization of *ca.* 14 minutes. This behaviour was
251 consistently observed across all CB % w/w concentrations (Figure S1 of Supporting Information),
252 and reported also in previous works (Martini et al., 2005b; Singh et al., 2002). The sheared
253 crystallization of CB/HOSO mixtures was thoroughly investigated in a recent publication,
254 reporting that cocoa butter crystallized as spherical aggregates of crystalline nanoplatelet (CNPs)
255 in the $\beta(V)$ form (Metilli et al., 2021) (Figure 5).

256 It is hypothesized, however, that CB first nucleated as a metastable polymorph (α or β') and then
257 transformed into the $\beta(V)$ structure during the experiments. It might be that the change in
258 compressibility and/or density associated to the formation of a liquid crystal structure – most likely
259 the α polymorph – were too small to be detected by the acoustic probe used in this work (Ladd
260 Parada et al., 2019). On the other hand, the nucleation and the growth of the $\beta(V)$ crystals and the

261 consequent development of the fat crystal network were clearly detected in both the velocity of
262 sound and acoustic attenuation (at 129 minutes). As the velocity of sound depends strongly on the
263 temperature, the first derivative with respect to temperature was calculated to better discriminate
264 the effect of crystal nucleation on this acoustic parameter (Figure 4b). Before the appearance of
265 fat crystals, when the change in the velocity of sound was only dependent on the temperature, the
266 calculated first derivative was zero; whereas, upon growth of the CB crystal network, the value of
267 this parameter changed significantly. Variations in the first derivative occurred at the same time
268 with the increase of the acoustic attenuation, which was caused by (a) scattering by fat crystals and
269 (b) additional attenuation mechanisms associated with the space filling interconnected fat crystals,
270 which also affected the overall compressibility of the system through the appearance of an
271 additional ‘frame modulus’ (Povey, 2017). Finally, fat crystal nucleation might release a high
272 amount of latent heat of solidification. In the case of the experiment of Figure 4a, such exothermic
273 process increased the process temperature from 3.2 °C to 5.65 °C (130-137 minutes). While this
274 temperature perturbation did not affect the signal from the turbidity probe or the acoustic
275 attenuation, it did affect the velocity of sound, which is strongly dependent on the sample
276 temperature.

277 After nucleation of the $\beta(V)$ polymorph, the crystallization process of Figure 4a proceeded until
278 275 minutes (region III), when the sample temperature reached *ca.* 1.5 °C, which corresponded to
279 the thermal equilibrium of the whole setup. In this time the acoustic attenuation kept increasing,
280 following a similar trend to the light absorbance. The velocity of sound also increased, but mostly
281 due to the change in temperature. Nevertheless, it is worth noticing in Figure 4b that the appearance
282 of fat crystals determined an increase in the noise of the first derivative of the velocity of sound,
283 albeit its mean value was still around zero.

284 After reaching equilibrium at around 275 minutes, the sample was heated back to 45 °C (region
285 IV). A focus on this region of the experiment is displayed in Figure 4c. In the heating step between
286 1.5 °C to 15 °C (from 280 minutes to 315 minutes), a decrease in the velocity of sound linearly
287 proportional to the decrease in temperature was observed. At the same time, a moderate decrease
288 in the acoustic attenuation happened, potentially linked to a decrease in the *SFC%* of the
289 crystallized sample.

290 Further increase in the sample temperature (from 315 to 330 minutes, 15 °C to 25 °C) resulted in
291 the complete melting of the fat crystalline network, which was evident in the sharp increase in
292 light transmittance and in the decrease in light absorbance, as well as acoustic attenuation. It is
293 worth noticing that both techniques detected full dissolution at the same time, around 327 minutes.
294 The velocity of sound presented a steeper decline in correspondence to the full melting; this was
295 clearly observable in the calculated first derivative.

296 Upon complete remelting of the sample (330 minutes – 350 minutes) all parameters returned to
297 their values prior to crystallization.

298 This set of experiments showed that the tested acoustic probe could be used to monitor
299 crystallization processes, although it seemed less sensitive than light turbidimetry to the detection
300 of early nucleated crystals, perhaps due to their liquid crystalline nature.

301 Experiments carried out with a higher weight % of CB showed similar trends for the acoustic and
302 light signals. The velocity of sound of the crystallized oleogels at different % w/w of added CB,
303 between 5 and 35°C, is shown in Figure 6.

304 In agreement with previous literature (McClements & Povey, 1992), the velocity of sound of the
305 crystallized oleogels increased, for the same range of temperatures, with increasing CB % w/w
306 (approximately by 10 m/s every 2 % of CB). From Figure 6 it can be noted that, between 20 and

307 25°C, the velocity of sound of all samples decreased steeply, due to the oleogels melting. It can be
308 appreciated that such decrease occurred at lower temperatures for lower CB concentrations, in
309 accordance with the lower melting point of the oleogels. Once liquid, the oleogels then displayed
310 the same velocity of sound of the sunflower oil.

311 The acoustic attenuation measured at equilibrium also increased with the amount of CB contained
312 in the oleogel, as shown in **Table 1**. In fact, higher concentrations of crystalline solids scattered
313 more sound and attenuated it. The relatively large standard deviation of the acoustic attenuation
314 for the 9% CB w/w sample, and its non-linear increase with higher concentrations of CB w/w,
315 however, prompts further work to establish a more robust relationship with the amount of solid fat
316 in the sample. In fact, the relationship between acoustic attenuation, *SFC*(%) and the crystal size
317 and shape is challenging to elucidate (Martini et al., 2005a).

318 The solid fat content (*SFC*%) of the CB/HOSO samples as a function of temperature was measured
319 with *p*NMR at the end of the crystallization step (Figure 7). Samples were collected directly from
320 the vessel to ensure direct comparison with the performed experiments.

321 By inspecting the *SFC*% values at 5 °C, it can be noted that all samples displayed a lower *SFC*%
322 compared to the total amount of added cocoa butter. This is because the main triacylglycerides
323 species that are solid at ambient temperature, 1,3-dipalmitoyl-2-oleoyl-glycerol (POP), 1,3-
324 distearoyl-2-oleoyl-glycerol (SOS) and 1-palmitoyl-2-oleoyl-3-stearoyl-glycerol (POS),
325 constitute about 80% w/w of cocoa butter, while the remaining 20% comprises mono- and di-
326 glycerides, phospholipids, sterols and free fatty acids that are liquid at ambient conditions (Dimick,
327 1991). The *SFC*(%) values were fitted using a Gompertz-type model, similar to the one described
328 in Farmani (2015) (Equation 6):

$$SFC(\%)(T, CB) = (b_0 + b_1 CB) e^{-e^{\frac{-(T-(b_{01}+(b_{11}CB))}{c}}}} \quad (\text{Eq. 6})$$

329 where T is the sample temperature, CB is the weight % of added cocoa butter, and $b_0 = 1.24$, $b_1 =$
 330 0.73 , $b_{01} = 13.48$, $b_{11} = 0.39$ and $c = -4.66$ are coefficient determined empirically. The fit enabled
 331 calculation of the $SFC(\%)$ as a function of temperature and CB concentration, which was used as
 332 a response matrix in the development of predictive models in the next section.

333

334 **3.2 Solid fat content predicted by Regression Learner model**

335 The measured $SFC(\%)$ with $pNMR$, and the predicted $SFC(\%)$ obtained with the Regression
 336 Learner models is displayed in Figure 8.

337 It can be noticed how the Linear model showed inaccuracies both when the sample was in the
 338 melted state (high temperatures), as well as in its crystallized phase, at all concentrations. This
 339 could be ascribed to the non-linear dependence of the $SFC(\%)$ with respect to temperature, as
 340 already highlighted in Figure 7. When considering the Fine Tree model, the accuracy generally
 341 improved, however still displaying some errors in predicting the $SFC(\%)$ of the oleogels, in
 342 particular between 15 and 25 °C. Finally, the GPR model showed the best predictive accuracy, for
 343 all samples and temperatures, with an RMSE value almost one order of magnitude lower compared
 344 to the other two models. Such improvement could stem from the similarity between the Gompertz-
 345 type $SFC(\%)$ dependence with temperature (Equation 6) and the gaussian-type distribution
 346 function (also exponential). Therefore, the GPR model was selected to predict the SFC% evolution
 347 during fat crystallization, as shown in Figure .

348

349 The increase in the predicted value of the $SFC\%$ in the oleogel matched the increase in the acoustic
 350 attenuation at 130 minutes, reaching 5% over few minutes and then levelling to a value of about

351 7.6%, very close to the equilibrium *SFC%* at such temperature (as shown in Figure 7). During the
352 heating phase, the *SFC%* started decreasing, falling sharply to 0% when the temperature was raised
353 above 20 °C and remaining constant thereafter, until the end of the experiment. Therefore, in
354 contrast with previous research, the approach presented in this work only requires measuring
355 velocity of sound, the temperature, and the *SFC(%)* measured with *p*NMR on samples on the
356 concentration of interest. The *SFC(%)* is then rapidly and accurately predicted from the ultrasonic
357 probe data under realistic operating conditions (*i.e.*, under shear and with large sample volumes).
358 The predicted *SFC%* for the samples at different CB % was plotted as a function of temperature
359 in Figure .

360 By inspecting the cooling profile, it can be noted that crystal growth, signalled by the increase in
361 *SFC%*, occurred at higher crystallization temperatures for oleogels containing higher % of CB, as
362 also reported previously in Metilli et al. (2021) for this type of system. Whereas, by inspecting the
363 heating profile, the *SFC%* decreased with the temperature with the same trend observed with
364 *p*NMR. The estimated values of *SFC%* at 5 °C during heating were 7.3, 8.7, 10.2 and 11.7% for
365 the 9, 11, 13 and 15% CB samples, respectively. These values are very close to the equilibrium
366 *SFC%* measured with *p*NMR at the same temperature (7.6, 8.5, 10.3 and 11.7%) indicating the
367 reliability of the predictive model built. Furthermore, both *p*NMR and acoustic spectroscopy
368 showed agreement that at 25 °C all samples returned to the full liquid state.

369 This work presents a prototype of an acoustic in situ probe, coupled with a reliable machine
370 learning-based predictive model, for online monitoring of oleogels crystallization. The probe could
371 provide useful quantitative information on the evolution of crystallization processes in an
372 industrial setting with minimal investment cost and calibration experiments. Furthermore, due to
373 the versatility of acoustic probes, the design of the hardware could be optimized in order to allow

374 effective measurements even in different fluid-dynamic environment (e.g., different crystallizers
375 designs, commercial tempering equipment).

376

377 **4. Conclusions**

378 In this work, the crystallization of cocoa butter–based oleogels was characterized qualitatively and
379 qualitatively using a custom-built immersion probe based on pulsed acoustic spectroscopy. The
380 *SFC%* of the oleogel during crystallization was estimated through a predictive model developed
381 with supervised machine learning. Such method uses the acoustic parameters (*i.e.*, velocity of
382 sound) collected from the immersion probe, the sample temperature and composition, and the
383 *SFC%* measured with *p*NMR. The predicted *SFC%* and its evolution during the shear
384 crystallization of the CB/HOSO mixtures was in agreement with the nucleation and development
385 of crystalline fat, as corroborated by light turbidimetry and acoustic attenuation. A comparison
386 between several predictive models showed that Gaussian Process Regression model was the most
387 accurate in describing the *SFC%* both prior and during crystallization. The *SFC%* value increased
388 steeply during crystal growth, with a final value close to 80% by weight of the added cocoa butter
389 in the mixture, with a similar trend to the acoustic attenuation. The *SFC%* then returned to 0%
390 close to the melting point of the oleogel, in agreement with the melting profile measured with
391 *p*NMR. Moreover, this work highlighted that turbidimetry was more sensitive in detecting the
392 nucleation of lipid crystals, whereas the acoustic probe was more responsive to the crystal growth
393 process. This difference could be ascribed to the liquid-crystalline nature of the metastable lipid
394 polymorph that developed during nucleation, for which the change in density and compressibility
395 may be too small to be measured by the current acoustic probe. Using a different frequency
396 transducer might increase the sensitivity of the ultrasonic probe to crystal nucleation; however,

397 this might result in excessive signal attenuation at equilibrium conditions, at which the *SFC*%
398 needs to be calculated. In summary, the results presented in this work demonstrate the feasibility
399 of implementing acoustic probes as PAT tools, in combination with supervised machine learning,
400 to improve the oleogel crystallization yield through the timely and accurate monitoring of the
401 *SFC*%.

402 ASSOCIATED CONTENT

403

404 **Supporting Information.**

405 PAT tools plot of 9, 11, 13 and 15% w/w CB in HOSO samples focused on nucleation of CB
406 crystals (Figure S1).

407 AUTHOR INFORMATION

408

409 **Corresponding Author**

410 Prof. Elena Simone

411 Elena.simone@polito.it

412

413 **Author Contributions**

414 The manuscript was written through contributions of all authors. All authors have given approval
415 to the final version of the manuscript.

416

417 **Funding Sources**

418 Centre for Doctoral Training in Soft Matter and Functional Interfaces (Grant ref. no.
419 EP/L015536/1).

420 Royal Society (Grant ref. no. INF\R2\192018).

421 Royal Academy of Engineering (Grant ref. no. IF/192031).

422 **ACKNOWLEDGMENTS**

423 The authors would like to acknowledge the Engineering and Physical Sciences Research Council
424 funded Centre for Doctoral Training in Soft Matter and Functional Interfaces, grant ref. no.
425 EP/L015536/1 as well as Nestlé PTC Confectionery (York, UK) for the pulsed NMR analysis, and
426 the financial and writing support. E.S. also acknowledges Royal Society (Grant ref. no.
427 INF\R2\192018) and Royal Academy of Engineering (Grant ref. no. IF/192031) for additional
428 funding.

429 **ABBREVIATIONS**

430 CB cocoa butter, GPR gaussian process regression, HOSO high oleic sunflower oil, ML machine
431 learning, SFC solid fat content, PAT process analytical technologies, *p*NMR pulsed nuclear
432 magnetic resonance.

433 **REFERENCES**

434 Agrawal, S. G., & Paterson, A. H. J. (2015). Secondary Nucleation: Mechanisms and Models.
435 *Chemical Engineering Communications*, 202(5), 698–706.
436 <https://doi.org/10.1080/00986445.2014.969369>

437 Rigolle, A., Van Den Abeele, K. and Foubert, I. (2018). Conventional and New Techniques to
438 Monitor Lipid Crystallization. In *Crystallization of Lipids*, K. Sato

439 (Ed.). <https://doi.org/10.1002/9781118593882.ch17>

440 Binks, B. P., & Vishal, B. (2021). Particle-stabilized oil foams. *Advances in Colloid and Interface*
441 *Science*, 291, 102404. <https://doi.org/10.1016/j.cis.2021.102404>

442 Birkhofer, B. H., Jeelani, S. A. K., Windhab, E. J., Ouriev, B., Lisner, K.-J., Braun, P., & Zeng,
443 Y. (2008). Monitoring of fat crystallization process using UVP–PD technique. *Flow*
444 *Measurement and Instrumentation*, 19(3–4), 163–169.
445 <https://doi.org/10.1016/j.flowmeasinst.2007.08.008>

446 Bosnić, Z., & Kononenko, I. (2009). An overview of advances in reliability estimation of
447 individual predictions in machine learning. *Intelligent Data Analysis*, 13(2), 385–401.
448 <https://doi.org/10.3233/IDA-2009-0371>

449 Bostijn, N., Hellings, M., Van Der Veen, M., Vervaet, C., & De Beer, T. (2018). In-line UV
450 spectroscopy for the quantification of low-dose active ingredients during the manufacturing
451 of pharmaceutical semi-solid and liquid formulations. *Analytica Chimica Acta*, 1013, 54–62.
452 <https://doi.org/10.1016/j.aca.2018.02.007>

453 Bowler, A. L., Bakalis, S., & Watson, N. J. (2020). Monitoring Mixing Processes Using Ultrasonic
454 Sensors and Machine Learning. *Sensors*, 20(7), 1813. <https://doi.org/10.3390/s20071813>

455 Bowler, A. L., & Watson, N. J. (2021). Transfer learning for process monitoring using reflection-
456 mode ultrasonic sensing. *Ultrasonics*, 115(May), 106468.
457 <https://doi.org/10.1016/j.ultras.2021.106468>

458 Brun, M., Delamplé, M., Harte, E., Lecomte, S., & Leal-Calderon, F. (2015). Stabilization of air
459 bubbles in oil by surfactant crystals: A route to produce air-in-oil foams and air-in-oil-in-

460 water emulsions. *Food Research International*, 67, 366–375.
461 <https://doi.org/10.1016/j.foodres.2014.11.044>

462 Cerdeira, M., Candal, R.J., Herrera, M. L. (2004). Analytical Techniques for Nucleation Studies
463 in Lipids : Advantages and Disadvantages. *Journal of Food Science*, 69(9), R185–R191.

464 Chaleepa, K., Szepes, A., & Ulrich, J. (2010). Metastable zone determination of lipid systems:
465 Ultrasound velocity versus optical back-reflectance measurements. *European Journal of*
466 *Lipid Science and Technology*, 112(5), 565–573. <https://doi.org/10.1002/ejlt.200900225>

467 Chávez, M., Sosa, V., & Tsumura, R. (1985). Speed of sound in saturated pure water. *Journal of*
468 *the Acoustical Society of America*, 77(2), 420–423. <https://doi.org/10.1121/1.391861>

469 Co, E. D., & Marangoni, A. G. (2012). Organogels: An alternative edible oil-structuring method.
470 *JAACS, Journal of the American Oil Chemists' Society*, 89(5), 749–780.
471 <https://doi.org/10.1007/s11746-012-2049-3>

472 Dimick, P. S. (1991). Principles of cocoa butter crystallization. *Manufacturing Confectioner*,
473 71(5), 115–125.

474 Duprat-De-Paule, S., Guilbot, J., Roso, A., Cambos, S., & Pierre, A. (2018). Augmented bio-based
475 lipids for cosmetics. *OCL - Oilseeds and Fats, Crops and Lipids*, 25(5).
476 <https://doi.org/10.1051/ocl/2018036>

477 Fairley, P., & McClements, D. J. (1992). Frequency scanning ultrasonic pulse echo reflectometer.
478 *Ultrasonics*, 30(6), 403–405.

479 Farmani, J. (2015). Modeling of solid fat content of chemically interesterified fully hydrogenated
480 soybean oil and canola oil blends as a function of temperature and saturated fatty acids.

481 *Journal of Food Measurement and Characterization*, 9(3), 281–289.
482 <https://doi.org/10.1007/s11694-015-9233-8>

483 Fernández-Moya, V., Martínez-Force, E., & Garcés, R. (2000). Identification of triacylglycerol
484 species from high-saturated sunflower (*Helianthus annuus*) mutants. *Journal of Agricultural*
485 *and Food Chemistry*, 48(3), 764–769. <https://doi.org/10.1021/jf9903861>

486 Foubert, I., Fredrick, E., Vereecken, J., Sichien, M., & Dewettinck, K. (2008). Stop-and-return
487 DSC method to study fat crystallization. *Thermochimica Acta*, 471(1–2), 7–13.
488 <https://doi.org/10.1016/j.tca.2008.02.005>

489 Goibier, L., Pillement, C., Monteil, J., Faure, C., & Leal-Calderon, F. (2019). Emulsification of
490 non-aqueous foams stabilized by fat crystals: Towards novel air-in-oil-in-water food colloids.
491 *Food Chemistry*, 293, 49–56. <https://doi.org/10.1016/j.foodchem.2019.04.080>

492 Hansen, T. B., Simone, E., Nagy, Z., & Qu, H. (2017). Process Analytical Tools to Control
493 Polymorphism and Particle Size in Batch Crystallization Processes. *Organic Process*
494 *Research and Development*, 21(6), 855–865. <https://doi.org/10.1021/acs.oprd.7b00087>

495 Heymans, R., Tavernier, I., Dewettinck, K., & Van der Meeren, P. (2017). Crystal stabilization of
496 edible oil foams. *Trends in Food Science and Technology*, 69, 13–24.
497 <https://doi.org/10.1016/j.tifs.2017.08.015>

498 Himawan, C., Starov, V. M., & Stapley, A. G. F. (2006). Thermodynamic and kinetic aspects of
499 fat crystallization. *Advances in Colloid and Interface Science*, 122, 3–33.
500 <https://doi.org/10.1016/j.cis.2006.06.016>

501 Hussin, A. B. B. H., & Povey, M. J. W. (1984). A study of dilatation and acoustic propagation in

502 solidifying fats and oils: II. Experimental. *Journal of the American Oil Chemists' Society*,
503 61(3), 560–564. <https://doi.org/10.1007/BF02677032>

504 Jaeggi, A., Rajagopalan, A. K., Morari, M., & Mazzotti, M. (2021). Characterizing Ensembles of
505 Platelike Particles via Machine Learning. *Industrial & Engineering Chemistry Research*,
506 60(1), 473–483. <https://doi.org/10.1021/acs.iecr.0c04662>

507 Jose, J., & Netto, G. (2019). Role of solid lipid nanoparticles as photoprotective agents in
508 cosmetics. *Journal of Cosmetic Dermatology*, 18(1), 315–321.
509 <https://doi.org/10.1111/jocd.12504>

510 Kloek, W., Walstra, P., & Van Vliet, T. (2000). Nucleation kinetics of emulsified triglyceride
511 mixtures. *JAOCs, Journal of the American Oil Chemists' Society*, 77(6), 643–652.
512 <https://doi.org/10.1007/s11746-000-0104-7>

513 Ladd Parada, M., Povey, M. J., Vieira, J., Rappolt, M., & Ries, M. E. (2019). Early stages of fat
514 crystallisation evaluated by low-field NMR and small-angle X-ray scattering. *Magnetic
515 Resonance in Chemistry*, 57(9), 686–694. <https://doi.org/10.1002/mrc.4860>

516 Lipp, M., Simoneau, C., Ulberth, F., Anklam, E., Crews, C., Brereton, P., ... Wiedmaier, C.
517 (2001). Composition of genuine cocoa butter and cocoa butter equivalents. *Journal of Food
518 Composition and Analysis*, 14(4), 399–408. <https://doi.org/10.1006/jfca.2000.0984>

519 Martini, S., Bertoli, C., Herrera, M. L., Neeson, I., & Marangoni, A. (2005a). Attenuation of
520 ultrasonic waves: Influence of microstructure and solid fat content. *JAOCs, Journal of the
521 American Oil Chemists' Society*, 82(5), 319–328. <https://doi.org/10.1007/s11746-005-1073->

523 Martini, S., Bertoli, C., Herrera, M. L., Neeson, I., & Marangoni, A. (2005b). In situ monitoring
524 of solid fat content by means of pulsed nuclear magnetic resonance spectrometry and
525 ultrasonics. *JAOCs, Journal of the American Oil Chemists' Society*, 82(5), 305–312.
526 <https://doi.org/10.1007/s11746-005-1071-8>

527 McClements, D. J. J., & Povey, M. J. W. (1988). Ultrasonic velocity measurements in some liquid
528 triglycerides and vegetable oils. *Journal of the American Oil Chemists' Society*, 65(11),
529 1787–1790. <https://doi.org/10.1007/BF02542383>

530 McClements, D. J., & Povey, M. J. W. (1992). Ultrasonic analysis of edible fats and oils.
531 *Ultrasonics*, 30(6), 383–388. [https://doi.org/10.1016/0041-624X\(92\)90094-3](https://doi.org/10.1016/0041-624X(92)90094-3)

532 McCLEMENTS, D. J., & POVEY, M. J. W. (1987). Solid fat content determination using
533 ultrasonic velocity measurements. *International Journal of Food Science & Technology*,
534 22(5), 491–499. <https://doi.org/10.1111/j.1365-2621.1987.tb00514.x>

535 Metilli, L., Lazidis, A., Francis, M., Marty-Terrade, S., Ray, J., & Simone, E. (2021). The Effect
536 of Crystallization Conditions on the Structural Properties of Oleofoams Made of Cocoa Butter
537 Crystals and High Oleic Sunflower Oil. *Crystal Growth & Design*, 21(3), 1562–1575.
538 <https://doi.org/10.1021/acs.cgd.0c01361>

539 Miles, C. A., Fursey, G. A. J., & Jones, R. C. D. (1985). Ultrasonic estimation of solid/liquid ratios
540 in fats, oils and adipose tissue. *Journal of the Science of Food and Agriculture*, 36(3), 215–
541 228. <https://doi.org/10.1002/jsfa.2740360312>

542 Morris, L., Simone, E., Glover, Z. J., Powell, H., Marty-Terrade, S., Francis, M., & Povey, M. J.
543 (2021). Dynamic monitoring of glycine crystallisation with low power ultrasound reflection

544 spectroscopy. *Chemical Engineering Research and Design*, 170, 213–223.
545 <https://doi.org/10.1016/j.cherd.2021.04.003>

546 Ochsenein, D. R., Vetter, T., Schorsch, S., Morari, M., & Mazzotti, M. (2015). Agglomeration
547 of needle-like crystals in suspension: I. Measurements. *Crystal Growth and Design*, 15(4),
548 1923–1933. <https://doi.org/10.1021/acs.cgd.5b00094>

549 Patel, A. R., & Dewettinck, K. (2016). Edible oil structuring: An overview and recent updates.
550 *Food and Function*, 7(1), 20–29. <https://doi.org/10.1039/c5fo01006c>

551 Patel, D., Patel, B., & Thakkar, H. (2021). Lipid Based Nanocarriers: Promising Drug Delivery
552 System for Topical Application. *European Journal of Lipid Science and Technology*, 123(5),
553 1–12. <https://doi.org/10.1002/ejlt.202000264>

554 Povey, M. J. W. (2017). Applications of ultrasonics in food science - novel control of fat
555 crystallization and structuring. *Current Opinion in Colloid and Interface Science*, 28, 1–6.
556 <https://doi.org/10.1016/j.cocis.2016.12.001>

557 Pu, Y., Chaudhry, S., Parikh, M., & Berry, J. (2015). Drug Development and Industrial Pharmacy
558 Application of in-line viscometer for in-process monitoring of microcrystalline cellulose-
559 carboxymethylcellulose hydrogel formation during batch manufacturing Application of in-
560 line viscometer for in-process monitoring of microcrystalline cellulose-
561 carboxymethylcellulose hydrogel formation during batch manufacturing. *Drug Dev Ind*
562 *Pharm*, 41(1), 28–34. <https://doi.org/10.3109/03639045.2013.845837>

563 Rathore, A. S., Bhambure, R., & Ghare, V. (2010). Process analytical technology (PAT) for
564 biopharmaceutical products. *Analytical and Bioanalytical Chemistry*, 398(1), 137–154.

565 <https://doi.org/10.1007/s00216-010-3781-x>

566 Rios, R. V., Pessanha, M. D. F., Almeida, P. F. de, Viana, C. L., & Lannes, S. C. da S. (2014).
567 Application of fats in some food products. *Food Science and Technology (Campinas)*, 34(1),
568 3–15. <https://doi.org/10.1590/s0101-20612014000100001>

569 Salami, H., McDonald, M. A., Bommarius, A. S., Rousseau, R. W., & Grover, M. A. (2021). In
570 Situ Imaging Combined with Deep Learning for Crystallization Process Monitoring:
571 Application to Cephalexin Production. *Organic Process Research and Development*, 25(7),
572 1670–1679. <https://doi.org/10.1021/acs.oprd.1c00136>

573 Simone, E., Saleemi, A. N., & Nagy, Z. K. (2015). In situ monitoring of polymorphic
574 transformations using a composite sensor array of Raman, NIR, and ATR-UV/vis
575 spectroscopy, FBRM, and PVM for an intelligent decision support system. *Organic Process
576 Research and Development*, 19(1), 167–177. <https://doi.org/10.1021/op5000122>

577 Simone, Elena, Tyler, A. I. I., Kuah, D., Bao, X., Ries, M. E., & Baker, D. (2019). Optimal Design
578 of Crystallization Processes for the Recovery of a Slow-Nucleating Sugar with a Complex
579 Chemical Equilibrium in Aqueous Solution: The Case of Lactose. *Organic Process Research
580 & Development*, 23(2), 220–233. <https://doi.org/10.1021/acs.oprd.8b00323>

581 Singh, A. P., McClements, D. J., & Marangoni, A. G. (2002). Comparison of ultrasonic and pulsed
582 NMR techniques for determination of solid fat content. *JAOCS, Journal of the American Oil
583 Chemists' Society*, 79(5), 431–437. <https://doi.org/10.1007/s11746-002-0501-y>

584 Singh, A. P., McClements, D. J., & Marangoni, A. G. (2004). Solid fat content determination by
585 ultrasonic velocimetry. *Food Research International*, 37(6), 545–555.

586 <https://doi.org/10.1016/j.foodres.2003.12.010>

587 Szilágyi, B., & Nagy, Z. K. (2018). Aspect Ratio Distribution and Chord Length Distribution
588 Driven Modeling of Crystallization of Two-Dimensional Crystals for Real-Time Model-
589 Based Applications. *Crystal Growth & Design*, 18(9), 5311–5321.
590 <https://doi.org/10.1021/acs.cgd.8b00758>

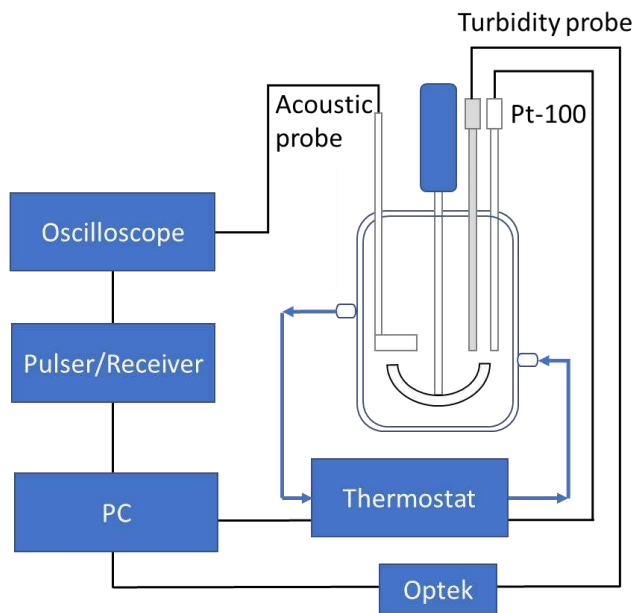
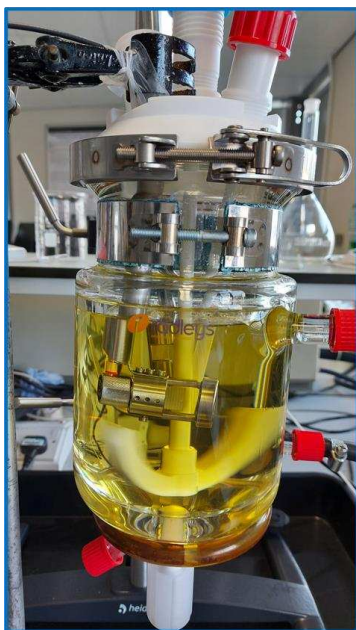
591 Tang, D., & Marangoni, A. G. (2008). Fractal dimensions of simulated and real fat crystal networks
592 in 3D space. *JAOCs, Journal of the American Oil Chemists' Society*, 85(6), 495–499.
593 <https://doi.org/10.1007/s11746-008-1237-7>

594 Titiz-Sargut, S., & Ulrich, J. (2003). Application of a protected ultrasound sensor for the
595 determination of the width of the metastable zone. *Chemical Engineering and Processing:
596 Process Intensification*, 42(11), 841–846. [https://doi.org/10.1016/S0255-2701\(02\)00215-5](https://doi.org/10.1016/S0255-2701(02)00215-5)

597 Wasalathanthri, D. P., Rehmann, M. S., Song, Y., Gu, Y., Mi, L., Shao, C., ... Li, Z. J. (2020).
598 Technology outlook for real-time quality attribute and process parameter monitoring in
599 biopharmaceutical development—A review. *Biotechnology and Bioengineering*, 117(10),
600 3182–3198. <https://doi.org/10.1002/bit.27461>

601

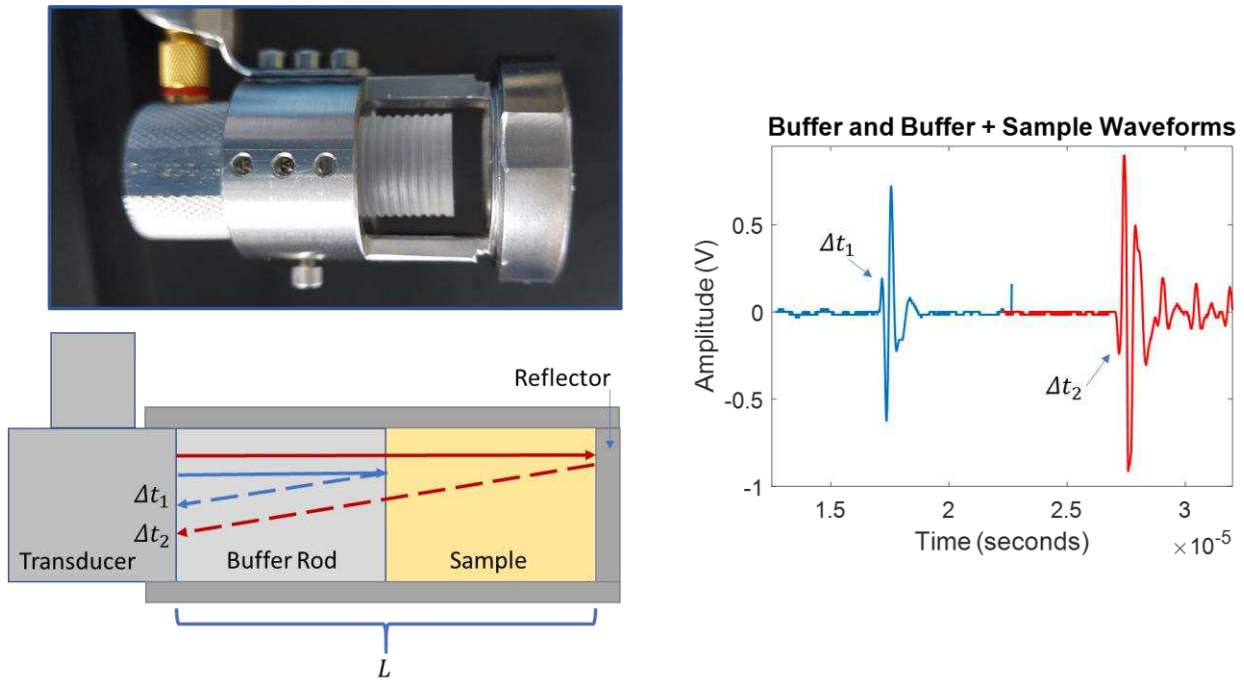
602



603

604 Figure 1. Crystallization vessel fitted with a Pt-100 thermocouple, the turbidity probe and the
605 custom ultrasound probe (left), schematic depiction of the rig used in this paper (right).

606



607

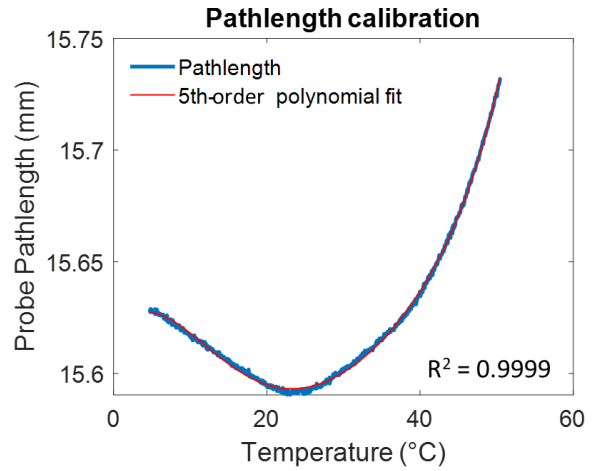
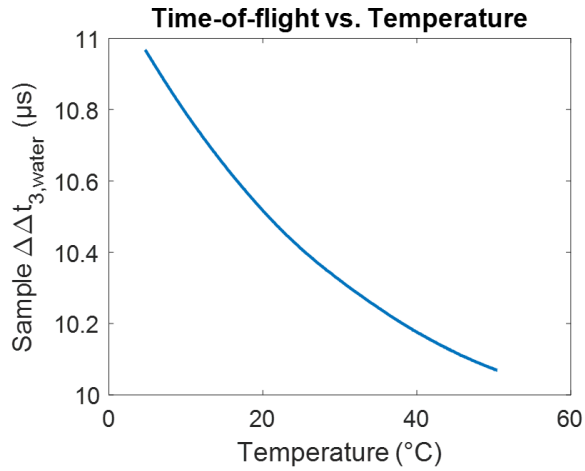
608 Figure 2. Schematic drawing of the custom acoustic probe (left) and the measured waveforms

609 obtained by the reflection of the buffer rod (blue), and buffer rod and sample (red) (right). Δt_1 and

610 Δt_2 represent the time-of-flight of the pulse travelling through the buffer rod and through the buffer

611 rod and sample, respectively.

612

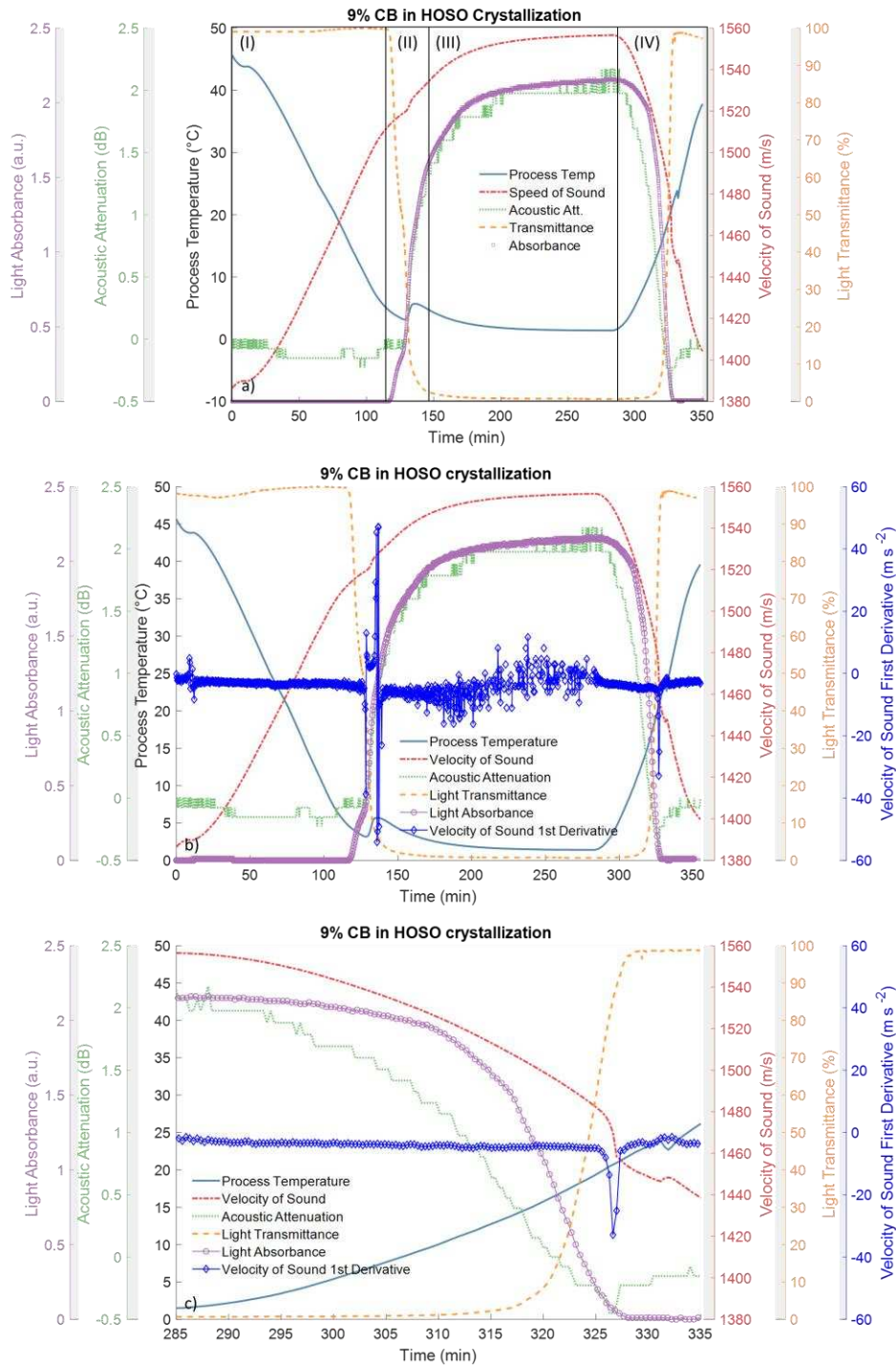


613

614 Figure 3. Measured time-of-flight in distilled water between 60 °C and 5 °C (left), calculated

615 sample path length and 5th-order polynomial fitting (right).

616



617

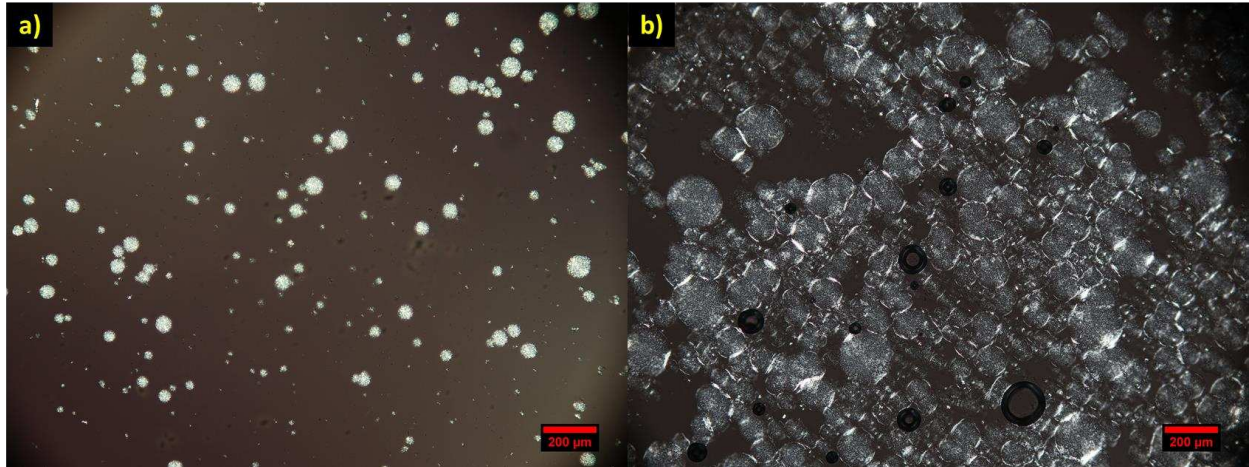
618 Figure 4. Process Analytical Technologies (PAT) tools plot of the crystallization of a 9% w/w CB

619 in HOSO blend (a). The different regions of the crystallization process are indicated with roman

620 numerals (I-IV). First derivative plot overlaid on the other PAT tools parameters (b) and

621 enlargement of the melting zone (c). Process temperature (-), velocity of sound (-·-), acoustic
622 attenuation (···), light transmittance (--), light absorbance (-o-) and first derivative of the velocity
623 of sound (-∅-) .

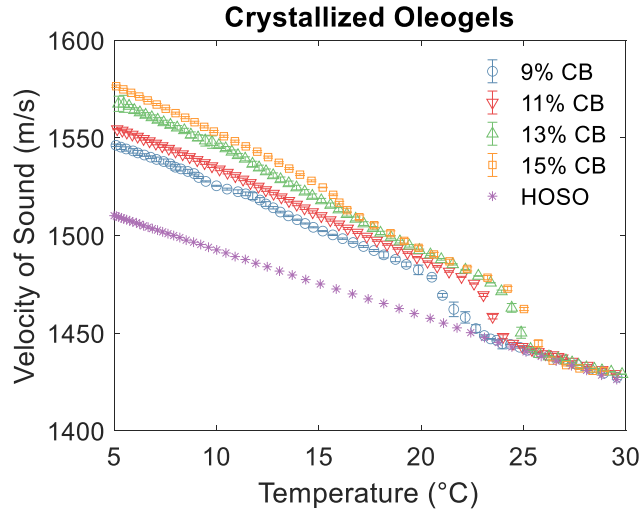
624



625

626 Figure 5. Polarized Light Microscopy (PLM) image of a 15% CB in HOSO mixture while
627 crystallizing under shear. Onset of nucleation (a) and formation of the spherical aggregates
628 network (b). Scale bar is 200 μm for both figures.

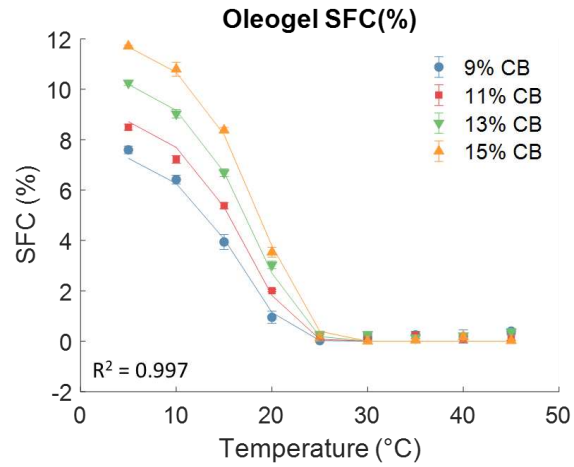
629



630

631 Figure 6. Velocity of sound of crystallized CB/HOSO oleogels between 5 and 35 °C. The error
632 bars show the standard deviation of three measurements for each concentration. The velocity of
633 sound of the pure HOSO phase is also plotted for reference.

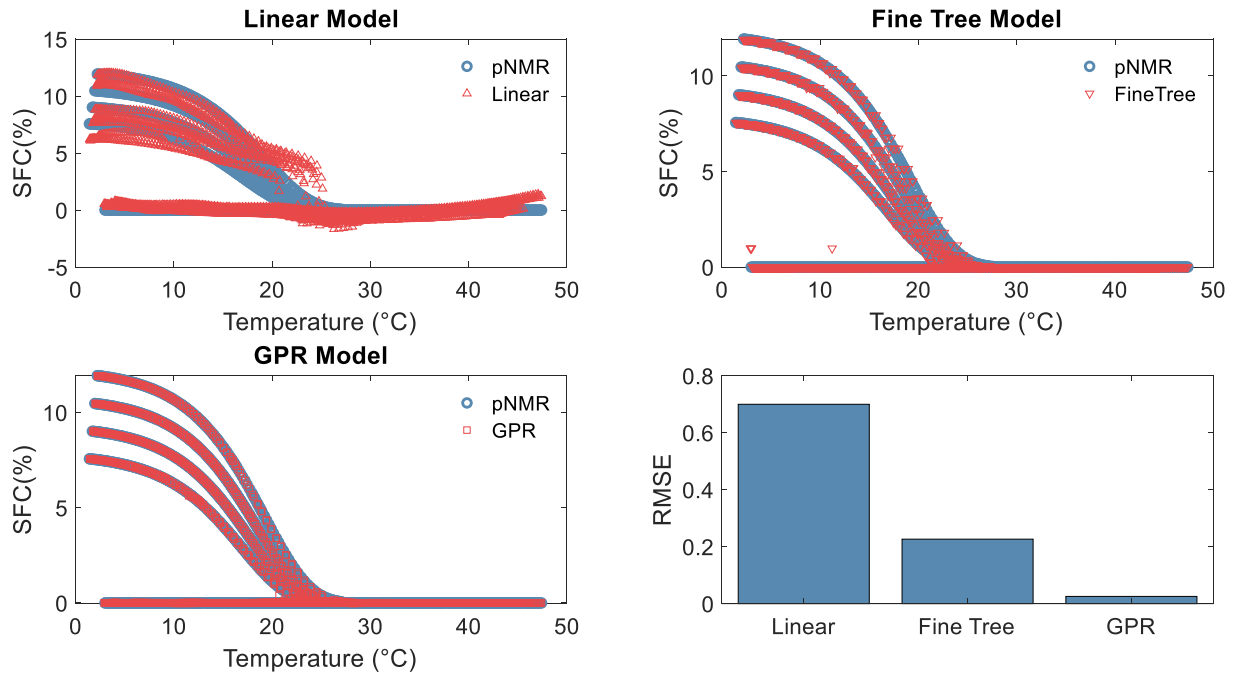
634



635

636 Figure 7. SFC% calculated with *p*NMR with respect to temperature for the different CB/HOSO
 637 blends. The datapoints were fitted using a Gompertz-type model, similar to the one described in
 638 Farmani (2015).

639



640

641 Figure 8. Predicted $SFC(\%)$ values obtained from the supervised-machine learning models,

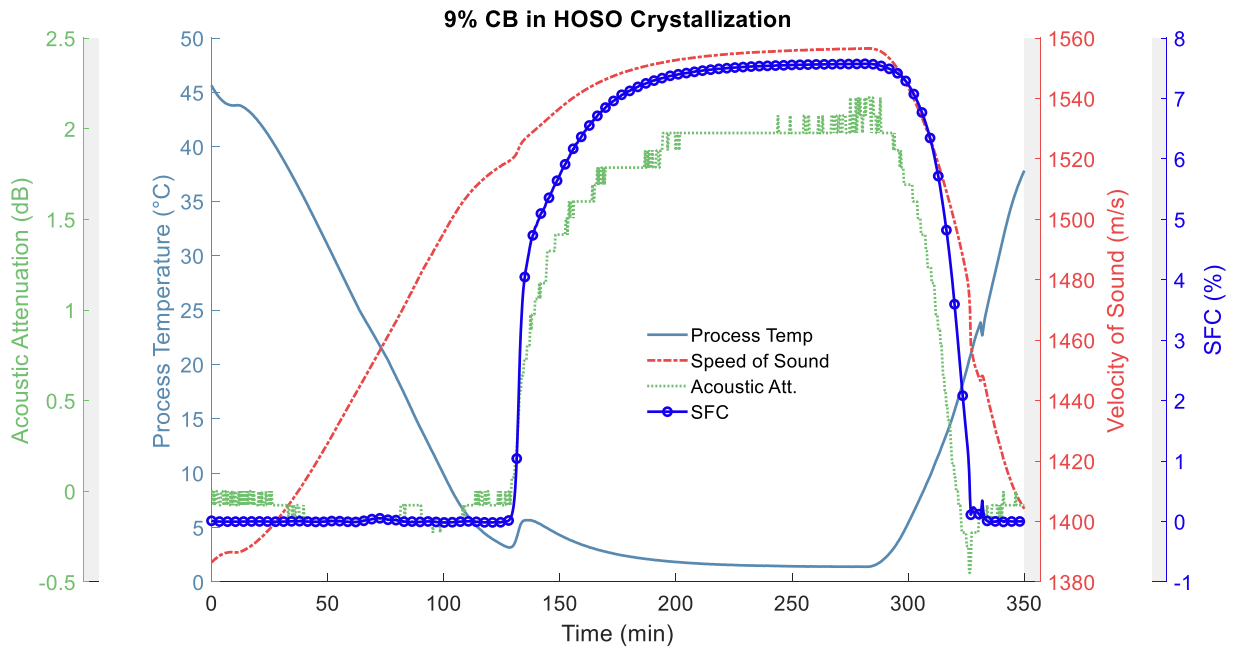
642 compared against the measured $SFC(\%)$ from $pNMR$ (blue circles) as a function of temperature:

643 a) Linear model (red upward triangles), b) Fine Tree model (red downward triangles), c) Gaussian

644 Process Regression (red squares) and d) histogram plot showing the RMSE values for each model.

645

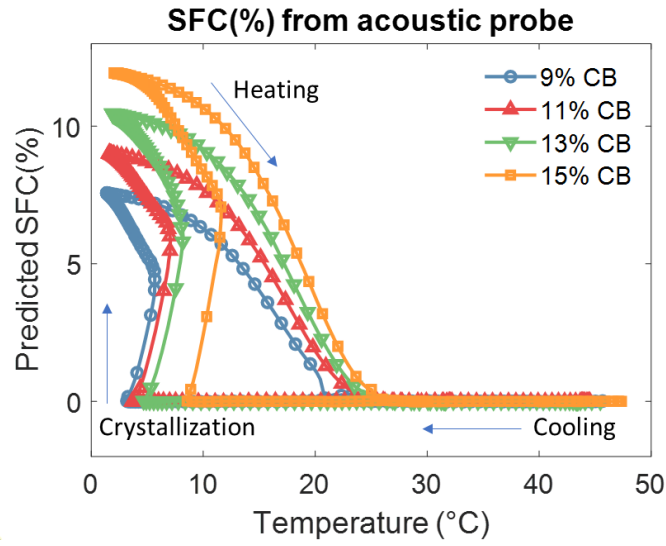
646



647

648 Figure 9. Process Analytical Technologies (PAT) tools plot of the crystallization of a 9% w/w CB
649 in HOSO blend. Process temperature (-), velocity of sound (-·-), acoustic attenuation (···), and
650 predicted SFC% with the GPR model (-o-).

651



652

653 Figure 10. Evolution of ultrasound predicted SFC% during cooling from 40 °C to 5 °C and heating

654 (5 °C to 40 °C) for oleogels containing different CB w/w %.

655

656

657 Table 1. Velocity of sound and acoustic attenuation for oleogel samples at the end of the
658 crystallization (5 °C).

CB % (w/w)	Velocity of Sound (5 °C) (m/s)	Acoustic Attenuation (5 °C) (dB)
9	1545.8 ± 2.2	2.25 ± 1.13
11	1555.1 ± 1.2	2.42 ± 0.09
13	1567.5 ± 6.5	2.61 ± 0.06
15	1578.6 ± 4.0	3.31 ± 0.42

659

660